Nonequilibrium phase transitions in feedback-controlled three-dimensional particle dynamics

Nonequilibrium phase transitions in feedback-controlled three-dimensional particle dynamics

Emilio N. M. Cirillo [1,*] Matteo Colangeli [2,†] Martin Kröger [3,4,‡] and Lamberto Rondoni [5,6,§]

[1]*Dipartimento di Scienze di Base e Applicate per L'Ingegneria, Sapienza Università di Roma, Via A. Scarpa 16, 00161 Rome, Italy*
[2]*Dipartimento di Ingegneria e Scienze dell'Informazione e Matematica, Università degli Studi dell'Aquila, via Vetoio, 67100 L'Aquila, Italy*
[3]*Department of Materials, Magnetism and Interface Physics, ETH Zurich, 8093 Zurich, Switzerland*
[4]*Department of Materials, Computational Polymer Physics, ETH Zurich, 8093 Zurich, Switzerland*
[5]*Dipartimento di Scienze Matematiche, Politecnico di Torino, Corso Duca degli Abruzzi 24, 10129 Torino, Italy*
[6]*INFN, Sezione di Torino, Via Pietro Giuria 1, 10125 Torino, Italy*

(Received 17 February 2023; accepted 27 September 2023; published 19 October 2023)

We consider point particles moving inside spherical urns connected by cylindrical channels whose axes both lie along the horizontal direction. The microscopic dynamics differ from that of standard 3D billiards because of a kind of Maxwell's demon that mimics clogging in one of the two channels, when the number of particles flowing through it exceeds a fixed threshold. Nonequilibrium phase transitions, measured by an order parameter, arise. The coexistence of different phases and their stability, as well as the linear relationship between driving forces and currents, typical of the linear regime of irreversible thermodynamics, are obtained analytically within the proposed kinetic theory framework, and are confirmed with remarkable accuracy by numerical simulations. This purely deterministic dynamical system describes a kind of experimentally realizable Maxwell's demon, that may unveil strategies to obtain mass separation and stationary currents in a conservative particle model.

DOI: 10.1103/PhysRevResearch.5.043063

I. INTRODUCTION

The study of the microscopic origin of nonequilibrium phase transitions is part of a prominent research endeavour [1,2], whose applications embrace various fields including, for instance, biology, crowd dynamics, and neuronal firing [3–7]. Given the complexity and variety of possible scenarios, exactly solvable models as well as experimental and numerical validations play an essential role in identifying general key ingredients underlying such nonequilibrium phenomena. Moreover, certain long considered gedanken experiments have recently been concretely realized, thanks to modern technology. In particular, Maxwell's demons have been implemented in classical systems using colloidal particles [8], a single-electron box [9], electrons in small transistors [10], a photodetector [11], DNA hairpin pulling experiments [12], cells [13], rotaxane molecules [14] as well as in stochastic quantum systems [15], superconducting circuit quantum electrodynamical systems [16], and optical lattices with ultracold atoms [17]. Of course, no violation of the second law of thermodynamics is implied. The implementation of the demon requires an external machinery that dissipates energy, or processes information, in such a way that the entropy of the universe substantially increases, while useful work is performed, e.g., by living organisms. Our paper links Maxwell's demons with the asymmetric diffusion of a single species of hard particles generated by the shape of the pores of a membrane separating two halves of a box [18]. The two ends of the pores have different cross section, and clogging of the particles entering their large side leads to an inhomogeneous (quasi)stationary density of matter. We propose a theoretical model for a variation of this experiment, in which particles can accumulate in one of the two halves of the container, giving rise to self sustained stationary currents. Since we consider point particles that do not interact with each other, we use a new kind of Maxwell's demon to implement the clogging phenomenon. We then develop a mathematical treatment based on a suitable stochastic process and on kinetic theory, accurately reproducing the results of direct and extensive numerical simulations. Experimental implications are discussed at the end of the paper.

II. THE 3D PARTICLE SYSTEM

Our model consists of N point particles moving with fixed speed v inside a bounded region $\Omega \subset \mathbb{R}^3$ constituted by two spherical urns of radius r, named urn 1 and urn 2, respectively located on the left and on the right of Fig. 1. These are connected by one central *active* and two peripheric *passive* coaxial cylindrical channels. Periodic boundary conditions are imposed, creating a closed loop. The widths and lengths of the channels are denoted, respectively, by w_a, ℓ_a (active channel) and by w_p, ℓ_p (passive channel).

*emilio.cirillo@uniroma1.it
†matteo.colangeli1@univaq.it
‡Corresponding author: mk@mat.ethz.ch
§lamberto.rondoni@polito.it

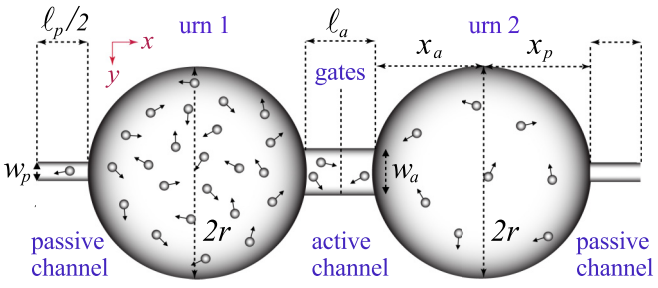

FIG. 1. A container Ω made of two 3D spherical urns and two coaxial cylindrical channels house N noninteracting particles. These move on straight lines from collision to collision with the walls of Ω, where they are elastically reflected. Periodic boundary conditions are imposed to form a circuit with the passive channel. Inside the active channel, a Maxwell's demon pushes particles back, when their number in a gate exceeds a given threshold.

The active channel is made of two identical gates, each connected to one urn, in which a mechanism called *bounce back* [19–21] operates as follows: Whenever the number of particles in a gate that are moving from the adjacent urn towards the more distant urn exceeds a fixed threshold Θ, the horizontal component of the velocity of such particles is inverted. This mechanism represents an externally tuned feedback control, introducing a short-range impulsive interaction among particles, that causes clogging. It amounts to a kind of Maxwell's demon operating symmetrically on the gates of the active channel.

Away from the gates, particles do not interact with one another, and move with fixed velocity $\mathbf{v}$, except at collision with the boundary $\partial\Omega$ of the container, where they are elastically reflected; i.e., their velocity changes to $\mathbf{v}' = \mathbf{v} - 2(\mathbf{v}\cdot\mathbf{n})\mathbf{n}$, where $\mathbf{n}$ denotes the outward normal to $\partial\Omega$ at the collision point, while their speeds $v = |\mathbf{v}| = |\mathbf{v}'|$ remain unaltered. Remarkably, the motion of a particle in one urn lies on a plane determined by its initial condition, while it draws a helix within the cylindrical channels, cf. Fig. 2 for a specific trajectory of a particle.

This dynamics is formally time reversible and conservative, although implementation requires an external energy consuming device, to count the particles in the active channel,

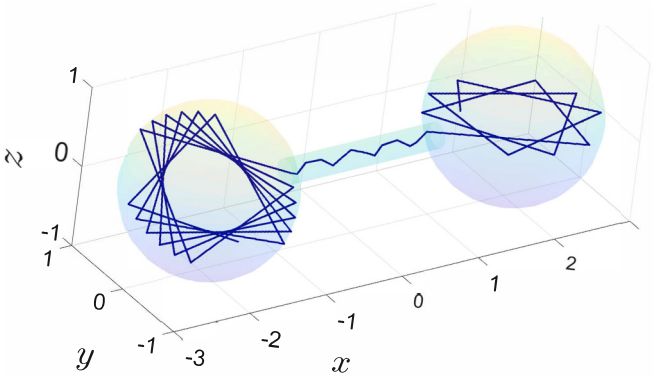

FIG. 2. Trajectory of a single particle in the absence of the bounce-back mechanism, for $r = v = 1$, $\ell_a = 1$, $w_a = 0.15$, and $w_p = 0$.

and to activate the bounce back. Nevertheless, the geometry of Ω combined with the bounce-back mechanism leads to a nonequilibrium phase transition in this model, in which different phases arise and can coexist. For sufficiently large N, and depending on the other parameters of the model, one observes: (a) an equilibrium phase, with particles evenly distributed in the two urns, and no net mass transport; (b) various stationary phases with inhomogeneous mass distributions, and a net particle current in the passive channel.

Mathematically, we found that the threshold Θ and two dimensionless parameters defined by Eqs. (2) and (3) quantitatively describe the corresponding phase diagram. The first is related to the ratio of the *effective* widths of the active and of the passive channels, i.e., of the fraction of the width of channels that can be crossed by particles coming from the nearest urn, while the second encodes relevant geometrical as well as kinetic length and time scales. These effective widths are determined by properly averaging over all possible lengths of the segments corresponding to the intersection of a generic plane of motion of a particle with the circular cross section of a cylindrical channel. Accounting for effective widths makes it possible to reduce the 3D billiard dynamics of the particles in the urns to a 2D problem, in which all particles in the urns reside on the same plane of motion and have access to the two channels equipped with the effective widths $\tilde{w}_a$ and $\tilde{w}_p$. Note that the underlying 3D dynamics of the original model is instead preserved in the channels, where the helical trajectory of a particle typically changes the plane of motion when the particle returns to an urn. This way, one can estimate the probability p_a (p_p) that a single particle enters the active (passive) channel in a fixed time interval $\delta > 0$. Kinetic theory arguments yield (Fig. 8 below)

$$\frac{p_a}{\delta} = \frac{\tilde{w}_a v}{\pi \tilde{A}_u}, \tag{1}$$

where $\tilde{A}_u$ is the near-circular cross-sectional area of a single urn (radius r) adjacent to channels of effective width $\tilde{w}_p$ and $\tilde{w}_a$ (see Appendix B for details). To first order in the ratio $w_a/2r < 1$ the latter quantity evaluates to $\tilde{w}_a \simeq \pi w_a^2/4\hat{w}$, with $\hat{w} = \max(w_a, w_p) \leqslant r$. Expressions analogous to Eq. (1) and $\tilde{w}_a$ hold for p_p and $\tilde{w}_p$. The first macroscopic parameter is the ratio of probabilities p_p and p_a, which, in the limit of small channel cross sections, equals the square of the ratio of w_p to w_a, viz.,

$$C \equiv \frac{p_p}{p_a} = \frac{\tilde{w}_p}{\tilde{w}_a} \simeq \left(\frac{w_p}{w_a}\right)^2. \tag{2}$$

Profiting, again, from the reduction of the billiard dynamics in the urns to a 2D problem, it is then straightforward to calculate the typical time τ_a a particle takes to cross one gate of the active channel, which is expressed by $\tau_a = \ell_a \pi/4v$ (Appendix C). Also, letting $\overline{N}_i$, with $i = 1, 2$, denote the steady-state number of particles in the ith urn, by using Eq. (1) and the expression of τ_a the typical number of particles that in a time τ_a enter the ith gate is given by $\lambda_i = \ell_a \tilde{w}_a \overline{N}_i/4\tilde{A}_u$. The second macroscopic parameter of our theory is the mean of λ_1 and λ_2, i.e.,

$$\lambda \equiv \frac{\lambda_1 + \lambda_2}{2} \approx \frac{\ell_a \tilde{w}_a}{\tilde{A}_u}\frac{N}{8}, \tag{3}$$

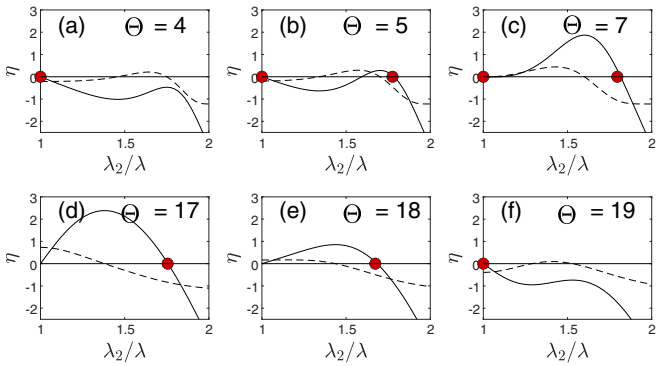

FIG. 3. Plots of η, Eq. (5), (solid line), and $\partial\eta/\partial\lambda_2$ (dashed line) at fixed $N = 2000$ and for fixed geometrical parameters, as functions of the normalized variable λ_2/λ and for different values of Θ in [(a)–(f)], with $r = v = 1$, $\ell_a = 1.5$, $w_a = 0.15$, $w_p = 0.05$, hence $\lambda \approx 14$ and $C = 1/9$. Zeroes of the black curve identify stationary states. Stable states, in the various panels, are identified by red circles.

the approximation being more accurate if a larger fraction of particles resides in the urns, i.e., when $\overline{N}_1 + \overline{N}_2$ is closer to N.

III. STEADY-STATE CURRENTS AND STABILITY CRITERIA

The stationary current per particle, which flows through the passive channel, can be estimated by exploiting the 2D analogy of the particle dynamics in the urns, which is achieved by replacing w_p with $\tilde{w}_p$. Applying the approach developed in [20] yields the expression $\overline{J}_p = (\tilde{w}_p v/\pi\tilde{A}_u)(\overline{N}_2 - \overline{N}_1)/N$, which is positive if particles move, on average, from urn 2 to urn 1. An expression for the stationary current flowing through the active channel is inherited from the above expression of $\overline{J}_p$ by properly accounting for the reflections caused by the feedback mechanism. Following again the derivation outlined in Ref. [20], in the limit $N \gg 1$ one finds

$$\overline{J}_a = \frac{\tilde{w}_a v}{\pi\tilde{A}_u}\left[\frac{\overline{N}_1\Gamma(\Theta,\lambda_1) - \overline{N}_2\Gamma(\Theta,\lambda_2)}{N\,\Gamma(\Theta,0)}\right], \tag{4}$$

where Euler's upper incomplete gamma function is defined by $\Gamma(y,x) = \int_x^\infty t^{y-1}e^{-t}\,dt$ for $y > 0$ and $\overline{J}_a$ is positive if particles move, on average, from urn 1 to urn 2. Note that $\overline{J}_p(\overline{N}_2 - \overline{N}_1) \geqslant 0$, i.e., particles in the passive channel move, on average, in the direction opposite to the stationary density gradient, as expected. The product $\overline{N}_i\Gamma(\Theta,\lambda_i)$ is instead monotonically decreasing with $\overline{N}_i$, which implies $\overline{J}_a(\overline{N}_2 - \overline{N}_1) \geqslant 0$. Thus $\overline{J}_a$ generates a kind of electromotive force for the current $\overline{J}_p$, preserving the density gradient. In a steady state, the currents $\overline{J}_p$ and $\overline{J}_a$ are equal. Introducing $\eta \equiv \tau_a(\overline{J}_a - \overline{J}_p)N$, the condition of stationarity translates into (Fig. 3)

$$\eta = \lambda_1\left[\frac{\Gamma(\Theta,\lambda_1)}{\Gamma(\Theta,0)} + C\right] - \lambda_2\left[\frac{\Gamma(\Theta,\lambda_2)}{\Gamma(\Theta,0)} + C\right] = 0, \tag{5}$$

The *mass spread* $\overline{\chi} \equiv |\overline{N}_2 - \overline{N}_1|/N = |\lambda - \lambda_2|/\lambda$ is an order parameter for our system. A linear relation links it to the absolute value of the steady-state current $\overline{J} = \overline{J}_a = \overline{J}_p$,

$$|\overline{J}| = \frac{p_p}{\delta}\,\overline{\chi} = \frac{v\,\tilde{w}_p}{\pi\tilde{A}_u}\,\overline{\chi}, \tag{6}$$

which resembles the linear laws of irreversible thermodynamics [22], if $\overline{\chi}$ plays the role of a thermodynamic force and the model parameters are fixed.

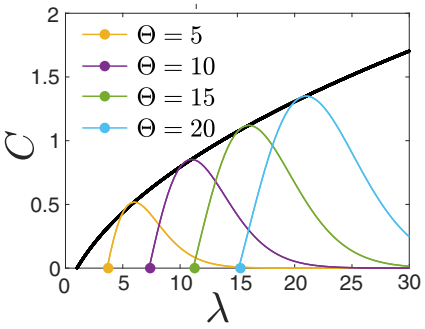

FIG. 4. Critical line in the (C,λ) plane, corresponding to the graph of the function $\mathcal{C}(\lambda - 1,\lambda)$ (black solid line), along with solutions of the interface equation (7) evaluated for different values of Θ (colored solid lines). The bullets correspond to analytical solutions of the same equation for $C = 0$.

Equation (5) shows that the *equilibrium state* $\overline{\chi} = 0$, i.e., $\lambda_2 = \lambda$, is always a solution. Further solutions arise, for certain values of the parameters, when η changes sign in intervals not containing λ. This amounts to *nonequilibrium* steady states with standing currents, if the passive channel has a nonvanishing effective width $\tilde{w}_p > 0$. In fact, one obtains $\overline{\chi} > 0$. In the cases in which η vanishes more than once for $\lambda_2 \in [\lambda, 2\lambda]$, one may ask which of the steady states of the model is stable. Given the smoothness of η, a state is linearly unstable (stable) if $(\partial\eta/\partial\lambda_2)$ is positive (negative). The stable steady states predicted by the theory are identified by red circles in Fig. 3. The points at which the derivative vanishes delimit their domain of stability, analogously to the spinodal curve of equilibrium statistical mechanics. This interface is obtained for $C = \mathcal{C}(\Theta,\lambda)$, where

$$\mathcal{C}(\Theta,\lambda) \equiv \frac{\lambda^\Theta e^{-\lambda}}{\Gamma(\Theta,0)} - \frac{\Gamma(\Theta,\lambda)}{\Gamma(\Theta,0)}. \tag{7}$$

For fixed Θ, the graph of $\mathcal{C}$ starts at the value -1 for $\lambda = 0$, it increases up to $\lambda = \Theta + 1$, and then decreases, asymptotically approaching zero. This implies that the interface equation has a single solution for $C = 0$, two solutions for $C \in (0, C_*)$, and no solutions for $C > C_*$, with C_* denoting a critical value of the parameter C. Thus, the condition for the existence of an interface reads $C \leqslant \mathcal{C}(\Theta, \Theta + 1)$, see Fig. 4. The "critical curve", in the parameter space spanned by the triple (Θ,λ,C) is identified by the two equations $\Theta_*{=}\lambda_*{-}1$ and $C_* = \mathcal{C}(\Theta_*,\lambda_*)$, while its projection on the (C,λ) space is shown in Fig. 4 along with several solutions of Eq. (7) evaluated at different values of Θ. A further theoretical line, called *coexistence line*, marks instead the presence of stationary nonequilibrium states. Such line, which shares some analogies with the binodal curves in the equilibrium theory of phase transitions, corresponds to the locus of points where both η and $(\partial\eta/\partial\lambda_2)$ simultaneously vanish for some $\lambda_2 \in (\lambda, 2\lambda]$.

In the (λ, Θ) space, with $C \in (0, C_*)$, our theory thus predicts a region of coexistence of equilibrium and nonequilibrium phases, in nice agreement with the results of the numerical simulations illustrated below.

IV. DYNAMICAL SIMULATIONS AND PHASE DIAGRAMS

Let us now present the results of an extensive set of numerical simulations of the 3D particle dynamics and compare them with the theoretical predictions.

Before the comparison can be made, one must consider that our probabilistic treatment of $\overline{J}_p$ and $\overline{J}_a$ excludes the particles trapped in one urn or never entering one of the two channels. As a matter of fact, in one urn, each particle moves in a plane determined by the initial conditions. If this plane does not intersect the opening of the wider channel, it does not intersect the opening of the narrower channel either, and the particle is trapped within that urn for all time. A particle may also travel between the two urns through only one of the two channels, avoiding the other one. Our theory only describes the set of particles that explore both urns and channels. The remaining particles, on the other hand, are uninteresting from the point of view of steady-state currents, and can be neglected.

To simulate only particles that visit all urns and channels, the initial datum has been carefully selected. To this end consider the angular velocity $\mathbf{L}(t) = \mathbf{r}(t) \times \mathbf{v}(t)$ of a particle with respect to the center of the urn at which it resides initially, where $\mathbf{r}(t)$ denotes the relative position vector of the particle at time t, and $\mathbf{v}(t)$ its velocity. During collisions of this particle along its trajectory through the whole system, $\mathbf{L}(t)$ tends to change its length and direction, except during its temporary residence within its initial urn. The horizontal component $L_x(t)$, however, is a conserved quantity, not only trivially inside urns, but also within the cylindrical channels. Therefore, for a particle initially in one urn to visit both channels in the course of time, the initial position $\mathbf{r}(0)$ and velocity $\mathbf{v}(0)$ must fulfill the following two geometrical inequalities at startup (derivation available in Appendix A):

$$|L_x(0)| \leqslant \frac{v}{2} \min(w_a, w_p) \text{ and } \frac{|L_x(0)|}{|\mathbf{L}(0)|} \leqslant \frac{1}{2r} \max(w_a, w_p). \tag{8}$$

In our simulations, the initial configuration of the particle system was prepared by initially placing $(1 - \chi(0))N/2$ particles in the urn 2 and the remaining ones in the urn 1. We assigned an initial position and velocity (with fixed speed v) to each particle using the following two-step procedure. One draws, first, the position $\mathbf{x}$ and velocity $\mathbf{v}$ of a particle from the uniform distributions in the physical and velocity space, respectively. Next, the random selection is accepted only if both inequalities in Eq. (8) hold; if not, the random drawing is reiterated until fulfillment of the two inequalities in Eq. (8).

Figure 5 shows the density plots in the two urns and both channels for different values of the parameter Θ, while the other parameters of the model are kept fixed. We recall that each particle moves on a fixed plane of motion in an urn; moreover the plane on which the particle resides generally changes anytime the particles access the same urn from one of the channels. Thus, for the sake of visualization, the various planes of motion related to the particle dynamics inside a given urn, have been all conveniently merged into a single plane orthogonal to the x axis. We observe that the various panels in Fig. 5 nicely match with the theoretical predictions illustrated in Fig. 3: homogeneous and inhomogeneous states are detected by the numerical simulations by varying the parameter Θ. Figure 5 also shows that the assumption regarding the uniformity of the single-particle density is only partially justified. At the center of each 2D circular urn, in Fig. 5, lies in fact a lighter gray-shaded concentric circle, whose size depends on the initial datum, which is traditionally called *caustic* in billiard dynamics. Indeed, single particles have dense trajectories in the circular urns, save for a concentric circle whose radius equals the sine of the angle formed by the velocity of the particle with the normal to the circle at the collision point on the boundary.

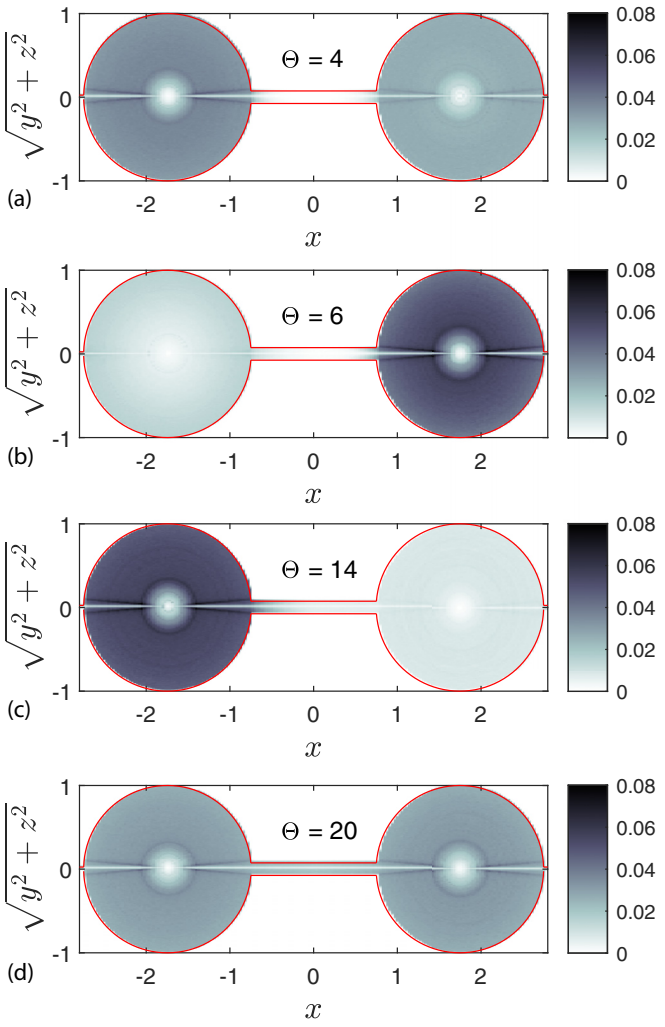

FIG. 5. Steady-state density profiles in the x-radial plane, using the parameters explored in Fig. 3, with $\ell_p = 0.1$, for (a) $\Theta = 4$, (b) $\Theta = 6$, (c) $\Theta = 14$, and (d) $\Theta = 20$.

The behavior of single realizations of the dynamics is illustrated in Fig. 6, which highlights the role of the parameter Θ in inducing the phase transition, at a fixed N. Specifically, Fig. 6(a) shows that both the theoretically predicted homogeneous and inhomogeneous steady states of Fig. 3 can be attained by tuning the threshold Θ, while leaving the number

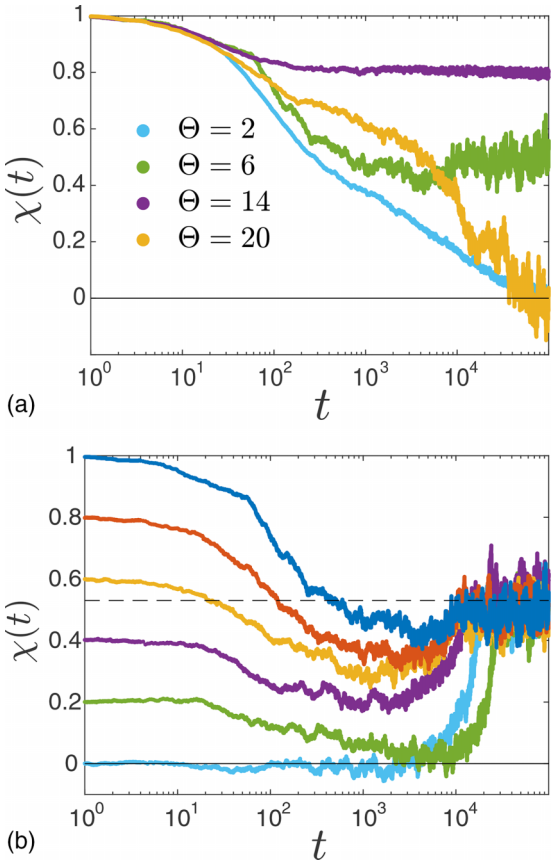

FIG. 6. (a) Dynamical behavior of $\chi(t)$ as a function of time for various Θ at $N = 2000$ and same geometry as in Fig. 3, supplemented by $\ell_a = 1.5$, $\ell_p = 0.1$ and $\chi(0) = 1$. (b) $N = 2000$, $\Theta = 6$, same geometry as in Fig. 3. The dashed black horizontal line marks the theoretical value.

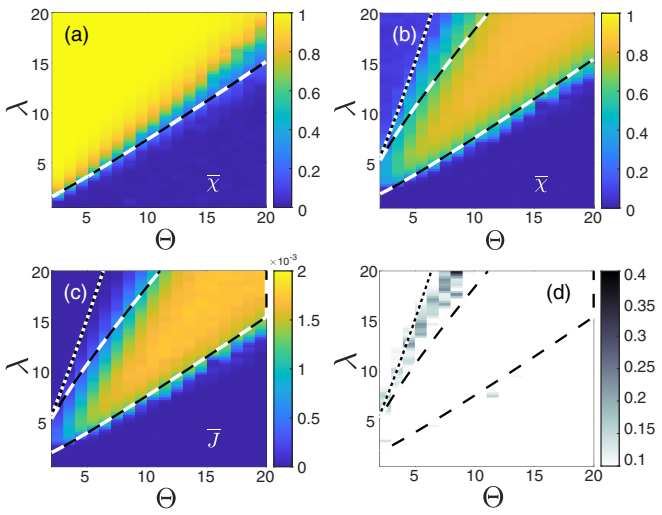

FIG. 7. Phase portrait of the 3D urn system in the (Θ, λ) plane, where Θ is integer valued. (a) Stationary values of the mass spread $\overline{\chi}$ for a system with a single channel ($C = 0$); (b) $\overline{\chi}$ for a system with two channels, and (c) the net current per particle $\overline{J}$ as functions of the parameters λ and Θ for $N = 2000$ and $C = 1/9$ in (b) and (c). The initial condition corresponds to $\chi(0) = 1$. The long dashed black-white line is the solution of the interface equation (7) (assuming continuous Θ), while the dotted line marks the onset of nonequilibrium states. The dotted line and the dashed line meeting on the left delimit the coexistence region. Panel (d) shows $\overline{\chi}(\chi(0) = 1) - \overline{\chi}(\chi(0) = 0)$.

of particles N and the other geometrical and kinetic parameters of the model (codified by the parameters λ and C) unchanged. Figure 6(b) shows various realizations of the dynamics starting from different values of $\chi(0)$, in a region of the parameter space where a unique (inhomogeneous) steady state is predicted by the theory. Our simulations hence provide numerical evidence that, away from the coexistence region, the same stationary state is reached regardless of the initial datum.

The phase diagrams resulting from our numerical simulations with N particles are portrayed in Fig. 7, which shows the phase diagram of the model and also evidences the excellent agreement between theoretical predictions and numerical results. Firstly, the simulations confirm the presence of two different branches of the interface, corresponding to solutions of Eq. (7), represented by the black-white long dashed lines. They identify the locus of points where the stability of the equilibrium states is broken. The existence of the two branches is in accord with the theory leading to Eq. (7) with $C \in (0, C_*)$. The white dotted lines, in Figs. 7(b) and 7(c), denote the coexistence line corresponding to the points where nonequilibrium states appear. Remarkably, our theory confirms the coexistence of equilibrium and nonequilibrium states, within the region delimited by the dotted and the dashed lines. Inside such coexistence region, the long-time behavior of the system depends sensibly on the initial configuration of the particles. This is highlighted in Fig. 7(d), which shows the difference $\overline{\chi}(\chi(0) = 1) - \overline{\chi}(\chi(0) = 0)$ between the values of the order parameter $\overline{\chi}$ computed from initial data corresponding to $\chi(0) = 1$ and to $\chi(0) = 0$, respectively. The nonzero values within the coexistence region in Fig. 7(d) confirms the presence of a metastable region and the breaking of the ergodic properties of the dynamics. It is also worth noticing that the direction of stationary currents, which arise for spontaneous symmetry breakings, cannot be foreseen *a priori*, since that direction is selected by fluctuations in the equilibrium state. The periodic motion of the particles within the system, which originates from the boundary conditions imposed at the endpoints of the passive channel, is also reminiscent of classical time crystals, whose existence was first conceived in [23].

V. CONCLUSIONS

In conclusion, we have proposed a kind of 3D Maxwell's demon, that can be experimentally interpreted in various ways; for instance, in terms of cold atoms, or of ratchet systems, in which nonequilibrium perturbations produce spatial asymmetries, despite being unbiased. Also, analogously to our findings, collective effects may arise as spontaneous symmetry breaking in symmetric nonequilibrium ratchet systems, cf. [24]. Our model may be especially intended as a variation of the experiment of [18], in which a second channel closing the box in a circuit is introduced, and the demon plays the role

of the membrane geometry. In our case, the moving particles are points, therefore clogging is obtained via the bounce-back mechanism, which is *per se* reversible. Moreover, our particles do not dissipate energy, exactly like the particles in the simulations of [18]. In the experiment, the dissipated energy is restored by vibrating the box. This way, a direct link between our model and a simple variation of the experiment of [18] is evidenced. One relevant difference is that the half box in which particles accumulate is macroscopically predictable in [18], as it is determined by the shape of the membrane. Our model is, instead, formally conservative and fully reversible. It produces nonequilibrium phase transitions, coexistence of different phases, and steady-state currents in a circuit, thanks to a spontaneous symmetry breaking nucleated by microscopic fluctuations. Therefore, the urn in which particles accumulate cannot be predicted on the macroscopic scale. Apart from this, the existence and stability of the different phases are fully analytically described by the theory, and illustrated in Figs. 3, 4, and 7.

Experimentally, our predictions may be tested in various ways. We point out that Fig. 5 reproduces the experimental set-up shown in Fig. 3 of [18], where no passive channel is present. In [18] the authors claim that the experimentally observed nonequilibrium states are induced by the interaction of the particles with each other and the walls of the asymmetric pores of the membrane. In our model, such short-range interactions are accounted for via the bounce-back mechanism, whose effects can be tracked analytically. We also remark that Maxwell's demon, codified by the bounce-back mechanism, can be experimentally realized in both classical and quantum systems, using modern technologies. For instance, in the case of cold atoms [25,26] particles could be counted by shining a laser at the gates of the active channel, which would operate a shutter when their number is above a threshold. Interesting applications are also provided by mobile robots [27–33], that could be counted through a photoelectric cell. Applications of our model to systems like those of [34] are possible as well.

ACKNOWLEDGMENT

This work has been performed under the auspices of Italian National Group of Mathematical Physics (GNFM) of the Istituto Nazionale di Alta Matematica (INdAM).

APPENDIX A: DERIVATION OF INEQUALITIES (8), INITIAL CONDITIONS

We start by proving that the horizontal x component of the angular velocity vector $\mathbf{L}(t) = \mathbf{r}(t) \times \mathbf{v}(t)$ of a particle, whose position vector with respect to the origin, and velocity vector are denoted by $\mathbf{r}(t)$ and $\mathbf{v}(t)$, is a conserved quantity. i.e., L_x does not change in the course of time, it remains unaffected during collisions with urns and channels, and during free flight between collisions. As the origin of the coordinate systems serves the point centered between the two active gates (Fig. 1), on the centerline of the cylindrical, active channel.

To prove this, it is sufficient to uniquely decompose $\mathbf{r}(t)$ into two parts. One that is parallel to the surface normal of the system during a collision, and otherwise arbitrary, and another one that is parallel to the horizontal x axis. Let $\hat{\mathbf{x}}$ denote the unit vector pointing in positive direction of the x axis. One possible decomposition is

$$\mathbf{r}(t) = \zeta(t)\hat{\mathbf{x}} + \mathbf{R}(t), \tag{A1}$$

where $\zeta(t)$ coincides either with the horizontal coordinate of an urn center if the particle resides in that urn, or with the horizontal coordinate $x(t)$ of the particle itself if the latter resides in a channel. This construction ensures that during a collision at $\mathbf{r}(t_c)$, at some collision time t_c, the vector $\mathbf{R}(t_c)$ is parallel to the surface normal $\mathbf{n}$ at the collision point. To be more specific, $\mathbf{R}(t_c) = r\mathbf{n}$ for a collision with an urn, and $\mathbf{R}(t_c) = (w_c/2)\mathbf{n}$ for a collision with channel $c \in \{a, p\}$, so that we can write $\mathbf{R}(t_c) = \xi(t_c)\mathbf{n}$.

During free flight, $\mathbf{r}(t)$ proceeds in direction of $\mathbf{v}(t)$, so that $\mathbf{L}(t)$ remains unchanged. During an elastic collision, the particle's velocity changes instantaneously by an amount $\Delta\mathbf{v} = -2\mathbf{v}_0 \cdot \mathbf{nn}$, where $\mathbf{v}_0$ stands for the velocity prior collision. The corresponding instantaneous change of the angular velocity vector is therefore

$$\begin{aligned}\Delta\mathbf{L} &= \mathbf{r}(t_c) \times \Delta\mathbf{v}_0 = (\zeta(t_c)\hat{\mathbf{x}} + \xi(t_c)\mathbf{n}) \times (-2\mathbf{v}_0 \cdot \mathbf{nn}) \\ &= -2\zeta(t_c)(\mathbf{v}_0 \cdot \mathbf{n})(\hat{\mathbf{x}} \times \mathbf{n})\end{aligned} \tag{A2}$$

This completes the proof, as the x component of $\hat{\mathbf{x}} \times \mathbf{n}$ is zero for any $\mathbf{n}$. To summarize, $L_x(t)$ is given by $L_x(0)$ as prepared at startup $t = 0$, while the other two components of $\mathbf{L}(t)$ are not conserved, as described by Eq. (A2).

To make sure that a particle, initially residing at some point $\mathbf{r}(0)$ with velocity $\mathbf{v}(0)$ somewhere inside the system, can reach both channels and urns in the course of time, its current or future plane of motion inside an urn must intersect at least with the larger of the two channels, the particle must be able to enter the channels, and it must have $|v_x(0)| \neq 0$, in case it is initially located in a channel. If these conditions are not met, the particle will stay in a region (urn or channel) for the rest of time. These considerations will give rise to the two nontrivial inequalities (8) as follows.

(i) The largest possible $|L_x(t)|$ that can be achieved inside a channel $c \in \{a, p\}$ is, e.g., realized when $v_z(t) = v$ and $y(t) = w_c/2$. This means that a particle can possibly be located at time t in channel c only if $|L_x(t)| \leqslant w_c v/2$. Because L_x is a conserved quantity, and because we require the particle be able to be located in both channels in the course of time, the inequality reads

$$|L_x(0)| \leqslant \frac{v}{2}\min(w_a, w_p). \tag{A3}$$

For the ease of presentation, within the main text we considered particles to be originally located in urns only, and redefined $\mathbf{L}(t) = \mathbf{R}(t) \times \mathbf{v}(t)$, which does not affect the value of L_x. This completes the proof of the first inequality (8).

(ii) The second inequality (8) is automatically fulfilled if a particle is initially located in a channel, so that we are left to prove it for the case of a particle that is initially located in an urn. A particle leaves an urn in the course of time, with a few exception of measure zero, if its plane of motion intersects with the smaller of the two channels. Inside an urn, a particle moves within a plane with constant normal vector $\boldsymbol{\ell}$ that is perpendicular to both $\mathbf{R}(t) = \mathbf{r}(t) - \zeta(t)\hat{\mathbf{x}}$ and $\mathbf{v}(t)$, i.e., it is given by $\boldsymbol{\ell}(t) = (\mathbf{R}(t) \times \mathbf{v}(t))/|\mathbf{R}(t) \times \mathbf{v}(t)|$. During free flight, and during a collision with the urn, $\Delta\boldsymbol{\ell} = \mathbf{0}$, because

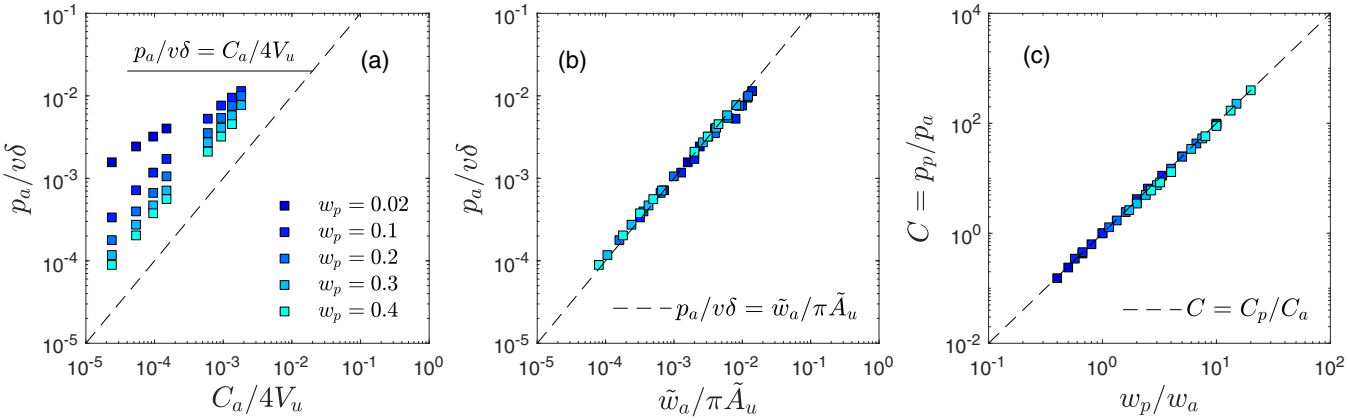

FIG. 8. Exact numerical results (symbols) in the absence of the bounce-back mechanism for $r = v = 1$, $\ell_a = 1$, $\ell_p = 0.1$, various w_a and w_p. Symbols with identical color have identical w_p, but different w_a. (a) $p_a/v\delta$ vs $C_a/4V_u$ shows that (B2) does not hold. (b) $p_a/v\delta$ vs $\tilde{w}/\pi\tilde{A}_u$ confirms the coefficient $\kappa = 1/\pi$, as well as the expressions for $\tilde{w}_c$ and $p_a/v\delta$, (B13), (B14), and (B15). (c) $C = p_p/p_a$ vs w_p/w_a is seen to be in agreement with $C = C_p/C_a = (w_p/w_a)^2$, (B16), and thus also in agreement with $C = \tilde{w}_p/\tilde{w}_a$.

$\mathbf{R}(t_c) \times \mathbf{n} = \mathbf{0}$. Moreover, this plane of motion contains the center of the urn, for which $\mathbf{R} = \mathbf{0}$. This implies that the plane of motion intersects channel c, if the plane normal encloses an angle with the x axis that exceeds a certain threshold, more precisely, if $|\boldsymbol{\ell}(0) \cdot \hat{\mathbf{x}}| = |\ell_x| \leqslant w_c/2x_c$. Because we need to only make sure that a particle does not stay in its initial urn forever, we end up with

$$|\ell_x(0)| \leqslant \frac{\max(w_a, w_p)}{2r}. \tag{A4}$$

Within the main text, for the ease of presentation, we assumed that particles are initially in urns, and defined $\mathbf{L}$ to be given by $\mathbf{L}(t) = \mathbf{R}(t) \times \mathbf{v}(t)$ so that $\mathbf{L}(t) = L(t)\boldsymbol{\ell}(t)$. This completes the proof of the second inequality (8).

Note that ℓ_x as opposed to L_x is not a conserved quantity but fortunately, inequality (A4) remains valid if $\ell_x(0)$ is replaced by $\ell_x(t)$, and if it was valid at startup, because particles entering an urn from channel c automatically fulfill $|\ell_x| \leqslant w_c/2x_c$. To summarize, the two inequalities ensure that a particle can reach both channels and urns in the course of time, and is not trapped in any of the urns. Even if a particle cannot leave its initial urn through the larger of the two channels, the larger channel can be reached after traveling through the other urn, and the inequality does not prevent this particle to reach any radial position at the channel entry of the smaller and larger channels. The more restrictive condition $|\ell_x(0)| \leqslant \min(w_a, w_p)/2r$ would ensure that a particle can leave its original urn through the smaller channel, but there is no need for such a more restrictive, and unnecessarily biasing, inequality.

APPENDIX B: DERIVATION OF EQS. (1) AND (2), PROBABILITIES p_a, p_p, AND EFFECTIVE CHANNEL DIAMETERS $\tilde{w}_a$, $\tilde{w}_p$

Here we compute p_a, namely the probability that a particle in an urn enters the adjacent gate of the active channel in a fixed time interval $\delta > 0$. This quantity is essential to predict the current $\overline{J}$ from the order parameter $\overline{\chi}$. The ratio $C = p_p/p_a$ of such probabilities for passive and active channels is furthermore relevant as it captures the qualitative behavior of the order parameter in the Θ–λ space. Two different routes are illustrated in the remainder of this Appendix. The first one (A) is based on naive standard kinetic theory arguments, but misses some of the peculiar geometric aspects of the considered 3D model. These are instead captured in the corrected derivation (B), which exploits *effective* cross sections and volumes. The failure of the classical approach and suitability of the refined approach is confirmed numerically by Fig. 8.

(A) Within the classical approach, we consider the case of a particle entering the left gate from the adjacent urn 1 (main text Fig. 1). Note that for symmetry reasons (the two urns are identical to one another, and so are the two gates), an identical expression for p_a is also obtained for particles in the urn 2 entering the right gate. We denote by $U \subset \Omega$ the region of the system corresponding to the urn 1 and we introduce the set $G = \{\mathbf{x} \in U \,|\, x \in [-\ell_a/2 - v_x\delta, -\ell_a/2]\}$. Furthermore, we call $S^2 = \{\mathbf{v} \in \mathbb{R}^3 \,|\, |\mathbf{v}| = v\}$ the sphere of radius v, and denote by S^2_+ the hemisphere corresponding to velocity directions $v_x \geqslant 0$. The probability p_a thus reads

$$p_a = \int_{S^2_+} d\mathbf{v} \int_G d\mathbf{x}\, \rho(\mathbf{x}, \mathbf{v}), \tag{B1}$$

where $\rho(\mathbf{x}, \mathbf{v})$ is the one-particle stationary probability density. Equation (B1) expresses the fact that only the particles residing in the interval $[-\ell_a/2 - v_x\delta, -\ell_a/2]$ inside the urn 1 and equipped with a horizontal component of the velocity $v_x \geqslant 0$ succeed to enter the adjacent gate within a fixed time interval δ. Still within the classical approach, we assume that the density $\rho(\mathbf{x}, \mathbf{v})$, with $\mathbf{x} \in U$ and $\mathbf{v} \in S^2$, is uniform over the entire phase space, namely we write $\rho(\mathbf{x}, \mathbf{v}) = (4\pi v^2 V_u)^{-1}$, with $V_u = \int_U d\mathbf{x}$ being the volume of one urn. To evaluate (B1), it then proves useful to turn into spherical coordinates, and rewrite the velocity as $\mathbf{v} = \mathbf{e}_x v\xi + \mathbf{e}_y v\sqrt{1-\xi^2}\cos\phi + \mathbf{e}_z v\sqrt{1-\xi^2}\sin\phi$ with $\xi \in [-1, 1]$ and $\phi \in [0, 2\pi]$.

Therefore (B1) evaluates to

$$p_a = \frac{C_a \int_0^1 d\xi \int_0^{v\xi\delta} dx \int_0^{2\pi} d\phi}{V_u \int_{-1}^1 d\xi \int_0^{2\pi} d\phi} = \frac{C_a v\delta \int_0^1 \xi d\xi}{V_u \int_{-1}^1 d\xi} = \frac{C_a v}{4V_u}\delta = \frac{\pi w_a^2 v}{16 V_u}\delta, \tag{B2}$$

where $C_a = \pi w_a^2/4$ is the geometric cross-section of the active channel, and

$$V_u = \frac{4\pi r^3}{3} - \frac{\pi}{3}\sum_{c\in\{a,p\}}(2r + x_c)(r - x_c)^2, \tag{B3}$$

the volume of a near-spherical urn, where $x_a^2 = r^2 - w_a^2/4$ and $x_p^2 = r^2 - w_p^2/4$ denote the squares of the distances between the center of an urn and the entrances of the active and the passive channels, respectively. An expression identical to (B2) can analogously be derived for p_p, upon replacing C_a with C_p. Hence, one finds

$$\frac{p_p}{p_a} = \frac{C_p}{C_a} \simeq \left(\frac{w_p}{w_a}\right)^2. \tag{B4}$$

Despite (B2) misses some relevant geometrical aspects of the 3D dynamics of the model, which makes the above expression for p_a inapplicable to capture the behavior of the current $\overline{J}$ even qualitatively, the final expression (B4) for the ratio turns out being correct, as the following refined calculation shows.

(B) The refined approach is necessary, because particles inside urns travel on fixed planes, whose orientation is generally determined by the angular momentum after the last collision with a channel wall, or the its position and velocity at startup $t = 0$, before having entered any channel. The above assumption of a uniform $\rho(\mathbf{x}, \mathbf{v})$ is therefore completely inappropriate to calculate p_a and p_p. Instead, the probability to enter a channel is determined by the width of the channel as seen within the cross section of the urn that carries the particle's trajectory. Because this width depends on the orientation of the angular velocities within bounds to be discussed later below, the channels will be characterized by their mean, effective widths $\tilde{w}_a$ and $\tilde{w}_p$. The urn's quasicircular cross section in a plane that contains the horizontal x axis equals the area of a 2D quasicircular urn and is given by

$$A_u(r, w_a, w_p) = \pi r^2 + \sum_{c\in\{a,p\}} \frac{w_c x_c}{2} - r^2 \sin^{-1}\left(\frac{w_c}{2r}\right). \tag{B5}$$

We wrote the structure of A_u explicitly, because we will reuse later the same expression to define an effective cross section

$$\tilde{A}_u = A_u(r, \tilde{w}_a, \tilde{w}_p), \tag{B6}$$

which is expressed in terms of the effective channel diameters $\tilde{w}_a$ and $\tilde{w}_p$, defined below. Since particles are noninteracting in the urns, and move along fixed planes of motion, the sought expression of p_a reduces to the expression obtained for a 2D system, provided *effective* channel diameters $\tilde{w}_a$ and $\tilde{w}_p$ are used in place of their geometric counterparts. We point out, in fact, that only those particles whose normal to the plane of motion is perpendicular to the x axis have access to the full channel diameters w_a and w_p to escape the urn. On the contrary, particles whose plane of motion intersects both channel entrances, typically exploit only a fraction of the channel diameters. Then, let, as in the preceding section, $\boldsymbol{\ell} = \ell_x\mathbf{e}_x + \ell_y\mathbf{e}_y + \ell_z\mathbf{e}_z$ denote the normalized vector normal to the plane of motion of a particle inside an urn. To derive the effective channel diameters we fix the initial conditions of the particle velocities such that the support of the ℓ_x component coincides with the interval $|\ell_x| \leqslant \hat{w}/2r$ [recall that we defined $\hat{w} = \max(w_a, w_p)$]. Furthermore, we here assume that, in the steady state, $\ell_x = \sin\alpha$ is uniformly distributed over its support.

Recalling that $x_c^2 = r^2 - w_c^2/4$, we have that $0 \leqslant \min(x_a, x_p)\tan\alpha \leqslant \hat{w}/2r$, and hence

$$0 \leqslant \tan^2(\alpha) = \frac{\ell_x^2}{1 - \ell_x^2} \leqslant \frac{\hat{w}^2}{4r^2 - \hat{w}^2}. \tag{B7}$$

We then denote by s_c the lengths of the secants of the plane of motion corresponding to α in the passive and in the active channels, respectively. By purely geometric considerations one finds

$$s_c = \sqrt{\frac{\max\left(0, w_c^2 - 4r^2\ell_x^2\right)}{1 - \ell_x^2}}, \tag{B8}$$

for $|\ell_x| \in [0, \hat{w}/2r]$ corresponding to $s_c \in [0, w_c]$. Note that s_c is an even function of ℓ_x, and is monotonically decreasing in $[0, \hat{w}/2r]$. Equation (B8) confirms that s_c equals zero on the interval $[w_c/2r, \hat{w}/2r]$ for the thinner of the two channels. We then denote by $\psi_a(s_a)$ and $\psi_p(s_p)$ the probability densities of the lengths s_a and s_p on the cross-sections of the active and passive channels, respectively. Exploiting the uniformity of ℓ_x over its support, we write

$$1 = \frac{2r}{\hat{w}}\int_0^{\hat{w}/2r} d\ell_x = \frac{2r}{\hat{w}}\int_0^{w_c/2r} d\ell_x + \frac{2r}{\hat{w}}\int_{w_c/2r}^{\hat{w}/2r} d\ell_x = \frac{\hat{w} - w_c}{\hat{w}} + \frac{2r}{\hat{w}}\int_0^{w_c/2r} d\ell_x, \tag{B9}$$

and therefore find for the probability densities

$$1 = \int_0^{w_c} \psi_c(s_c)\, ds_c = -\frac{2r}{\hat{w}}\int_0^{w_c}\left(\frac{d\ell_x}{ds_c}\right)ds_c + \int_0^{w_c}\frac{\hat{w} - w_c}{\hat{w}}\delta(s_c)\, ds_c, \tag{B10}$$

where the required ℓ_x as function of s_c is provided by Eq. (B8). The Dirac δ distribution reflects the contribution to $\psi_c(0)$ for the smaller of the two channels. Comparing the integrands in Eq. (B10) leads to

$$\psi_c(s_c) = \frac{2r}{\hat{w}}\frac{\left(4r^2 - w_c^2\right)s_c}{\left(4r^2 - s_c^2\right)^{3/2}\sqrt{w_c^2 - s_c^2}} + \frac{\hat{w} - w_c}{\hat{w}}\delta(s_c). \tag{B11}$$

With ψ_c at hand we can define and calculate the effective cross sections

$$\begin{aligned}\tilde{w}_c &= \int_0^{w_c} s_c\psi_c(s_c)\, ds_c \\ &= \frac{4r^2}{\hat{w}}E\left[\left(\frac{w_c}{2r}\right)^2\right] - \frac{\left(4r^2 - w_c^2\right)}{w_c}K\left[\left(\frac{w_c}{2r}\right)^2\right], \\ &= 2r\left\{\frac{2r}{\hat{w}}E\left[\left(\frac{w_c}{2r}\right)^2\right] - \frac{1 - (w_c/2r)^2}{w_c/2r}K\left[\left(\frac{w_c}{2r}\right)^2\right]\right\},\end{aligned} \tag{B12}$$

for $c \in \{a, p\}$, where $E(m)$ is the complete elliptic integral, and $K(m)$ the complete elliptic integral of the first kind. Since $y \equiv w_c/2r < 1$, this exact result (B12) can be further evaluated by Taylor expansion to yield

$$\tilde{w}_c = \frac{w_c}{\hat{w}}\left[\frac{2r}{y}\{E(y^2) - (1-y^2)K(y^2)\}\right] = \frac{w_c}{\hat{w}}\left[\frac{\pi}{2}ry + \frac{\pi}{16}ry^3 + \mathcal{O}(y^5)\right] = \frac{\pi}{4}\frac{w_c^2}{\hat{w}}[1 + \mathcal{O}(y^2)] \tag{B13}$$

for $c \in \{a, p\}$. The leading term is capturing the exact result up to high precision up to $y \approx 0.6$; for larger $w_c > r$, the exact Eq. (B12) can be used. We thus end up, upon writing down the result for both $\tilde{w}_a$ and $\tilde{w}_p$ separately, with

$$\tilde{w}_a \simeq \frac{\pi}{4}\frac{w_a^2}{\hat{w}}, \quad \tilde{w}_p \simeq \frac{\pi}{4}\frac{w_p^2}{\hat{w}}, \quad \hat{w} \equiv \max(w_a, w_p) \tag{B14}$$

for $\hat{w} \leqslant r$. The effective channel diameters are thus both smaller than the geometrical diameters and the effective diameter of the larger channel depends on the diameter of the smaller one.

The next step requires to adapt (B1) to a 2D urn system equipped with effective diameters $\tilde{w}_a$ and $\tilde{w}_p$. It is thus enough to replace the volume V_u by the area $\tilde{A}_u = A_u(r, \tilde{w}_a, \tilde{w}_p)$, the latter explicitly defined in (B5). With these replacements, (B1) can now be used to calculate the correct expressions of p_a and p_p for the 3D model. Since particles are independent in the urns and each one moves on a specific plane of motion, the evaluation of p_a can be carried out by adopting the 2D set-up considered in Refs. [19,20], by now using $\tilde{A}_u$ as the area of the urn and $\tilde{w}_a$ as the effective width of the active channel. We thus arrive at

$$p_a = \frac{\tilde{w}_a \int_{-\pi/2}^{\pi/2}\int_0^{v\delta\cos\phi} dxd\phi}{\tilde{A}_u \int_{-\pi}^{\pi} d\phi} = \frac{\tilde{w}_a v\delta \int_{-\pi/2}^{\pi/2}\cos(\phi)d\phi}{\tilde{A}_u \int_{-\pi}^{\pi} d\phi} = \frac{\tilde{w}_a v}{\pi\tilde{A}_u}\delta, \tag{B15}$$

where ϕ denotes the angle enclosed by the velocity vector with the unit vector pointing along the positive direction of the (horizontal) x axis. This completes the derivation of Eq. (1) in the main text. Note the qualitative difference between (B2) and (B15). It is important to stress that both the channel cross-section and the urn volume in (B15) have to be evaluated using $\tilde{w}_a$ and $\tilde{w}_p$ given by (B14). Finally, the probability p_p referring to the passive channel can then be obtained from (B15) upon replacing $\tilde{w}_a$ with $\tilde{w}_p$. Remarkably, using (B14) and (B15) we recover the earlier (B4), viz.,

$$C \equiv \frac{p_p}{p_a} = \frac{\tilde{w}_p}{\tilde{w}_a} \simeq \left(\frac{w_p}{w_a}\right)^2. \tag{B16}$$

The latter result highlights that the ratio of effective and geometric channel cross sections is basically identical for $\hat{w}/r < 0.6$. For larger channel diameters, the exact expressions for $\tilde{w}_a$ and $\tilde{w}_p$ given by (B13) can be used. This completes the derivation of Eq. (2) in the main text.

Figure 8(c) shows the excellent agreement between the analytical expression of C given in (B16) with the numerical evaluation of the same quantity through numerical simulations of the particle dynamics. Figures 8(a) and 8(b) confirm that the refined methodology (B) applies, while (A) fails.

APPENDIX C: DERIVATION OF τ_a

Another relevant ingredient of the theory is the typical time spent by a particle to cross one gate, denoted by τ_a. Estimating this quantity allows one to quantify the frequency of activation of the bounce-back mechanism in each gate of the active channel. To evaluate τ_a, we proceed by directly computing the average time spent by a particle coming from an urn in traversing one gate, until it reaches the center of the active channel. One thus finds

$$\tau_a = \mu\frac{\ell_a}{2v}, \qquad \text{with} \qquad \mu \equiv v\left|\left\langle v_x^{-1}\right\rangle_e\right|, \tag{C1}$$

where $\langle\cdot\rangle_e$ denotes a stationary average restricted to those particles equipped with horizontal component of the velocity $v_x > 0$ entering the left gate ($x \leqslant 0$) and $v_x < 0$ entering the right gate ($x > 0$). Namely, the average $\langle\cdot\rangle_e$ is taken, in each gate, over those particles, which *entered* a gate from the nearest urn and are thus moving toward the other gate. Then, relying again on the effective 2D nature of the particle dynamics in the urns that can be characterized via the effective channels widths $\tilde{w}_a$ and $\tilde{w}_p$, one readily finds $\mu = \pi/2$, i.e.,

$$\tau_a = \frac{\ell_a\pi}{4v}. \tag{C2}$$

[1] H. Hinrichsen, Non-equilibrium phase transitions, Physica A **369**, 1 (2006).

[2] M. Henkel, H. Hinrichsen, and S. Lübeck, *Non-Equilibrium Phase Transitions* (Springer, Dordrecht, 2008).

[3] A. Ghosh, D. De Martino, A. Chatterjee, M. Marsili, and B. K. Chakrabarti, Phase transitions in crowd dynamics of resource allocation, Phys. Rev. E **85**, 021116 (2012).

[4] S. Gupta, A. Campa, and S. Ruffo, Nonequilibrium first-order phase transition in coupled oscillator systems with inertia and noise, Phys. Rev. E **89**, 022123 (2014).

[5] M. A. Pietruszka, Non-equilibrium phase transition at a critical point of human blood, Sci. Rep. **11**, 22398 (2021).

[6] M. Fruchart, R. Hanai, P. B. Littlewood, and V. Vitelli, Non-reciprocal phase transitions, Nature (London) **592**, 363 (2021).

[7] H. F. W. Elleard, H. Holly, B. Sonya, and I. R. Fredrik, Phase transitions in biology: From bird flocks to population dynamics, Proc. R. Soc. B **288**, 20211111 (2021).

[8] S. Toyabe, T. Sagawa, M. Ueda, E. Muneyuki, and M. Sano, Experimental demonstration of information-to-energy conversion and validation of the generalized Jarzynski equality, Nat. Phys. **6**, 988 (2010).

[9] J. V. Koski, V. F. Maisi, T. Sagawa, and J. P. Pekola, Experimental observation of the role of mutual information in the nonequilibrium dynamics of a Maxwell demon, Phys. Rev. Lett. **113**, 030601 (2014).

[10] K. Chida, S. Desai, K. Nishiguchi, and A. Fujiwara, Power generator driven by Maxwell's demon, Nat. Commun. **8**, 15301 (2017).

[11] M. D. Vidrighin, O. Dahlsten, M. Barbieri, M. S. Kim, V. Vedral, and I. A. Walmsley, Photonic Maxwell's demon, Phys. Rev. Lett. **116**, 050401 (2016).

[12] M. Ribezzi-Crivellari and F. Ritort, Large work extraction and the Landauer limit in a continuous Maxwell demon, Nat. Phys. **15**, 660 (2019).

[13] S. Ito and T. Sagawa, Maxwell's demon in biochemical signal transduction with feedback loop, Nat. Commun. **6**, 7498 (2015).

[14] V. Serreli, C.-F. Lee, E. R. Kay, and D. A. Leigh, A molecular information ratchet, Nature (London) **445**, 523 (2007).

[15] B. Ahmadi, S. Salimi, and A. S. Khorashad, Irreversible work and Maxwell demon in terms of quantum thermodynamic force, Sci. Rep. **11**, 2301 (2021).

[16] Y. Masuyama, K. Funo, Y. Murashita, A. Nohuchi, S. Kono, Y. Tabuchi, R. Yamazaki, M. Ueda, and Y. Nakamura, Information-to-work conversion by Maxwell's demon in a superconducting circuit quantum electrodynamical system, Nat. Commun. **9**, 1291 (2018).

[17] A. Kumar, T.-Y. Wu, F. Giraldo, and D. S. Weiss, Sorting ultracold atoms in a three-dimensional optical lattice in a realization of Maxwell's demon, Nature (London) **561**, 83 (2018).

[18] R. S. Shaw, N. Packard, M. Schröter, and H. L. Swinney, Geometry-induced asymmetry diffusion, Proc. Natl. Acad. Sci. USA **104**, 9580 (2007).

[19] E. N. M. Cirillo, M. Colangeli, A. Muntean, O. Richardson, and L. Rondoni, Deterministic reversible model of non-equilibrium phase transitions and stochastic counterpart, J. Phys. A: Math. Theor. **53**, 305001 (2020).

[20] E. N. M. Cirillo, M. Colangeli, O. Richardson, and L. Rondoni, Deterministic model of battery, uphill currents, and nonequilibrium phase transitions, Phys. Rev. E **103**, 032119 (2021).

[21] E. N. M. Cirillo, M. Colangeli, A. Di Francesco, M. Kröger, and L. Rondoni, Transport and nonequilibrium phase transitions in polygonal urn models, Chaos **32**, 093127 (2022).

[22] S. R. de Groot and P. Mazur, *Non-Equilibrium Thermodynamics* (Dover Publications, New York, 2011).

[23] F. Wilczek, Classical time crystals, Phys. Rev. Lett. **109**, 160401 (2012).

[24] P. Reimann, Brownian motors: Noisy transport far from equilibrium, Phys. Rep. **361**, 57 (2002).

[25] V. Milner, J. L. Hanssen, W. C. Campbell, and M. G. Raizen, Optical billiards for atoms, Phys. Rev. Lett. **86**, 1514 (2001).

[26] A. Kaplan, M. Andersen, N. Friedman, and N. Davidson, Atom-optics billiards, in *Chaotic Dynamics and Transport in Classical and Quantum Systems*, NATO Science Series II: Mathematics, Physics and Chemistry, edited by P. Collet, M. Courbage, S. Metens, A. Neishadt, and G. Zalavsky (Springer, Berlin, 2003), Vol. 182, pp. 239–267.

[27] O. Çağırıcı, Y. Bahoo, and S. M. LaValle, Bouncing robots in rectilinear polygons, in *26th International Conference on Methods and Models in Automation and Robotics (MMAR)* (IEEE, 2022), pp. 193–198.

[28] A. Q. Nilles, I. Becerra, and S. M. LaValle, Periodic trajectories of mobile robots, in *2017 IEEE/RSJ International Conference on Intelligent Robots and Systems (IROS)* (IEEE, 2017), pp. 3020–3026.

[29] A. Q. Nilles, Y. Ren, I. Becerra, and S. M. LaValle, A visibility-based approach to computing non-deterministic bouncing strategies, Int. J. Robot. Res. **40**, 1196 (2021).

[30] L. Bobadilla, F. Martinez, E. Gobst, K. Gossman, and S. M. LaValle, Controlling wild mobile robots using virtual gates and discrete transitions, in *2012 American Control Conference (ACC)* (IEEE, 2012), pp. 743–749.

[31] G. DiBari, L. Valle, R. T. Bua, L. Cunningham, E. Hort, T. Venenciano, and J. Hudgings, Using hexbugs to model gas pressure and electrical conduction: A pandemic-inspired distance lab, Amer. J. Phys. **90**, 817 (2022).

[32] M. Paoluzzi, R. Di Leonardo, and L. Angelani, Self-sustained density oscillations of swimming bacteria confined in microchambers, Phys. Rev. Lett. **115**, 188303 (2015).

[33] W. Li, L. Li, Q. Shi, M. Yang, and N. Zheng, Spontaneous population oscillation of confined active granular particles, Soft Matter **18**, 5459 (2022).

[34] C. Gmachl, F. Capasso, E. Narimanov, J. U. Nockel, A. D. Stone, J. Faist, D. L. Sivco, and A. Y. Cho, High-power directional emission from microlasers with chaotic resonators, Science **280**, 1556 (1998).